Applications of advanced kinetic collisional radiative modeling and Bremsstrahlung emission to quantitative impurity analysis on the National Spherical Torus Experiment

J. M. Muñoz Burgos, K. Tritz, D. Stutman, R. E. Bell, B. P. LeBlanc, and S. A. Sabbagh

Citation: Physics of Plasmas **22**, 123301 (2015); doi: 10.1063/1.4936953
View online: http://dx.doi.org/10.1063/1.4936953
View Table of Contents: http://scitation.aip.org/content/aip/journal/pop/22/12?ver=pdfcov
Published by the AIP Publishing

Applications of advanced kinetic collisional radiative modeling and Bremsstrahlung emission to quantitative impurity analysis on the National Spherical Torus Experiment

J. M. Muñoz Burgos,[1,a)] K. Tritz,[1,b)] D. Stutman,[1,c)] R. E. Bell,[2,d)] B. P. LeBlanc,[2,e)] and S. A. Sabbagh[3,f)]
[1]*Department of Physics and Astronomy, Johns Hopkins University, Baltimore, Maryland 21218, USA*
[2]*Princeton Plasma Physics Laboratory, Princeton, New Jersey 08543, USA*
[3]*Columbia University, New York, New York 10027, USA*

(Received 29 September 2015; accepted 20 November 2015; published online 9 December 2015)

An advanced kinetic collisional radiative model is used to predict beam into plasma charge-exchange visible and extreme UV (XUV $\backsim 50 - 700$ Å) light emission to quantify impurity density profiles on NSTX. This kinetic model is first benchmarked by predicting line-of-sight integrated emission for the visible $\lambda = 5292.0$ Å line of carbon (C VI $n = 8 \rightarrow 7$), and comparing these predictions to absolute calibrated measurements from the active CHarge-Exchange Recombination Spectroscopy diagnostic (CHERS) on NSTX. Once benchmarked, the model is used to predict charge-exchange emission for the 182.1 Å line of carbon (C VI $n = 3 \rightarrow 2$) that is used to scale Bremsstrahlung continuum emission in the UV/XUV region. The scaled Bremsstrahlung emission is used as a base to estimate an absolute intensity calibration curve of a XUV Transmission Grating-based Imaging Spectrometer (TGIS) diagnostic installed on the National Spherical Torus Experiment (NSTX and upgrade NSTX-U). The TGIS diagnostic operates in the wavelength region $\backsim 50 - 700$ Å, and it is used to measure impurity spectra from charge-exchange emission. Impurity densities are estimated by fitting synthetic emission from the kinetic charge-exchange model to TGIS spectral measurements. © *2015 AIP Publishing LLC*. [http://dx.doi.org/10.1063/1.4936953]

I. INTRODUCTION

Monitoring and quantifying impurity elements such as Fe, Mo, W, etc., play an important part in fusion physics research.[1] High-*Z* elements have commonly been observed in tokamak plasmas,[2] and their quantification is important to prevent loss of power by radiation in burning plasmas. The upgrade on the National Spherical Torus Experiment (NSTX-U)[3] at the Princeton Plasma Physics Laboratory (PPPL) will eventually include the placement of Titanium-Zirconium-Molybdenum (TZM) alloy tiles on the lower divertor for high-*Z* wall studies.

In support of these studies, the Johns Hopkins University plasma spectroscopy group designed and built a Transmission Grating-based Imaging Spectrometer (TGIS). This diagnostic operated on NSTX in a survey mode to measure impurity lines from beam into plasma charge-exchange and Bremsstrahlung continuum emission, and it is scheduled to continue to operate on NSTX-U. The TGIS covers the XUV/VUV regions with a spectral window between $\backsim 50$ and 700 Å ($\delta\lambda/\lambda \backsim 3\%$ resolution), and a field of view of 22°, and 0.9 m $< R <$ 1.5 m ($\backsim 2.7$ cm of resolution).[1]

In order to expand the capabilities of the TGIS diagnostic to obtain quantitative impurity measurements, accurate beam into plasma charge-exchange modeling and absolute intensity calibration of the instrument are needed.

This paper first describes the adaptation of an already developed advanced kinetic collisional radiative model to predict beam into plasma charge-exchange impurity emission.[4,5] This model was first developed to determine atomic physics corrections to measured apparent plasma rotation velocities based on carbon charge-exchange emission at the DIII-D tokamak. In this work, the model is expanded to include in the kinetic collisional radiative model not only electron, but ion-impact excitation and ionization interactions that become important in the high-temperature/density core environment of NSTX. The model is used to predict line-integrated beam into plasma charge-exchange emission from different plasma impurity ions, including non-hydrogen-like systems. The model closely reproduces absolute intensity calibrated measurements from the active CHarge-Exchange Recombination Spectroscopy diagnostic (CHERS) that operates on a regular basis on NSTX. The CHERS diagnostic measures fully stripped carbon ion temperatures and densities, as well as rotation velocities from charge-exchange using the visible $\lambda = 5292.0$ Å line (C VI $n = 8 \rightarrow 7$).

In order to absolutely calibrate the TGIS instrument, the charge-exchange model is used to predict line integrated emission of the XUV 182.1 Å line (C VI $n = 3 \rightarrow 2$). This line is chosen due to its high intensity in the XUV, and the absence of other strong impurity lines around its wavelength. The predicted relative intensity of this line to the continuum is used to scale modeled Bremsstrahlung emission in the XUV/VUV range of the TGIS ($\backsim 50 - 700$ Å). The scaled Bremsstrahlung continuum emission is then used as a reference for absolute intensity calibration of the TGIS.

[a)]Electronic mail: jmunozbu@pppl.gov.
[b)]Electronic mail: ktritz@pppl.gov.
[c)]Electronic mail: dstutma1@jhu.edu.
[d)]Electronic mail: rbell@pppl.gov.
[e)]Electronic mail: leblanc@pppl.gov.
[f)]Electronic mail: sabbagh@pppl.gov.

Combining absolute calibrated spectral measurements from the TGIS with modeled charge-exchange and Bremsstrahlung continuum emission, quantitative impurity density radial profiles are estimated.

The paper is organized as follows: Section II describes the adaptation of the advanced kinetic collisional radiative model to predict charge-exchange emission,[4,5] followed by Section III which includes a summary of the neutral beam model employed to calculate beam deposition and penetration into the plasma.[6] Section IV contains a description of the atomic data employed in the kinetic model for different ion impurities. Section V benchmarks the modeled results by direct comparison to absolute intensity calibrated measurements of the $\lambda = 5292.0$ Å radial profiles from CHERS, as well as calculating a complete line-integrated carbon charge-exchange spectra. Section VI describes the absolute intensity calibration of the TGIS based on scaled Bremsstrahlung continuum emission,[7] and the quantification of impurity density radial profiles.

II. ADVANCED KINETIC COLLISIONAL RADIATIVE MODEL

An advanced kinetic collisional radiative model that includes gyro-orbit effects in charge-exchange impurity capture and emission was developed to determine plasma rotation velocities at the DIII-D tokamak.[4,5] In the present work, this model is adapted to predict charge-exchange emission from different impurity ions (both hydrogen-like and non-hydrogen-like) in order to quantify their local densities. This model does not take into account any impurity transport mechanisms, electrons are exchanged between the neutral beam and the local impurities that are already present, and therefore, their densities are quantified from the charge-exchange emission process. The question of how the impurities get to the measured location is dealt by the field of transport theory.[8]

The adapted model may include many populating mechanisms in the collisional-radiative system. These *nl*-terms/*nlj*-levels resolved mechanisms may be (but are not limited to):

- Spontaneous decay: $(A_{ml'\to nl}/A_{nl\to ml'})$
- Electron-impact excitation/de-excitation: $(q^e_{ml'\to nl}/q^e_{nl\to ml'})$
- Ion-impact excitation/de-excitation: $(q^i_{ml'\to nl}/q^i_{nl\to ml'})$
- Electron-impact ionization: (S^e_{nl})
- Ion-impact ionization: (S^i_{nl})

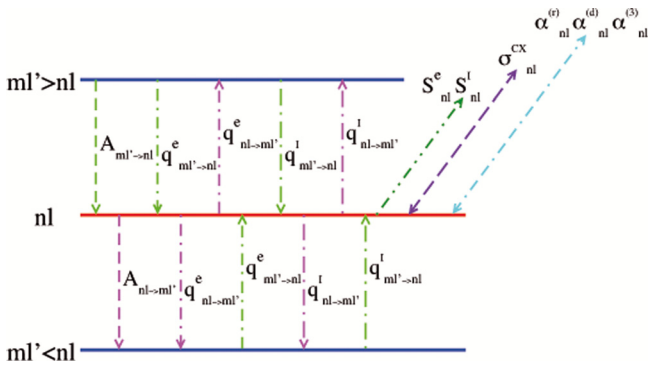

FIG. 1. Different populating/de-populating mechanisms for the nl^{th}-term of an ion in a plasma.

- Radiative recombination: $[\alpha^{(r)}_{nl}]$
- Dielectronic recombination: $[\alpha^{(d)}_{nl}]$
- Three-body recombination: $[\alpha^{(3)}_{nl}]$
- Charge-exchange: (σ^{CX}_{nl}).

Figure 1 illustrates different mechanisms that contribute to the population of the nl^{th} atomic term of an impurity ion, where *nl* represents the specific term that is described (*nlj* for a level), and ml' represents any higher or lower term from *nl*. Notice that other processes such as interactions with other ion impurities may also be included in the collisional-radiative formalism.

Electron and ion impact excitation and ionization rate coefficients are calculated by assuming *Maxwellian* distributions. For the impurity ions before a charge-exchange event, a shifted *Maxwellian* distribution with respect to the plasma rotation velocity is employed in the form[4]

$$f_i(\boldsymbol{v}-\boldsymbol{V}_r) = \frac{n_i}{\pi^{3/2}v_{th}^3}\, e^{-(\boldsymbol{v}-\boldsymbol{V}_r)^2/v_{th}^2}, \tag{1}$$

where $\boldsymbol{V}_r$ is the measured ion rotation velocity from CHERS, and the ion thermal velocity is represented by $v_{th} = \sqrt{2k_BT_i/m_i}$.

In order to account for all radiative and collisional couplings, as well as ion gyro-velocity effects in a charge-exchange event, the kinetic equation is solved. The different collisional processes (on the right hand side) are included in the form

$$\frac{\partial f_{nl}}{\partial t} + \boldsymbol{v}\cdot\nabla f_{nl} + \frac{Z_i e}{m_i}(\boldsymbol{E}+\boldsymbol{v}\times\boldsymbol{B})\cdot\nabla_{\boldsymbol{v}} f_{nl} = \sum_{nl\neq ml'}\left(A_{ml'\to nl} + n_e q^e_{ml'\to nl} + n_i q^i_{ml'\to nl}\right) f_{ml'} - \Big\{ n_e S^e_{nl} + n_i S^i_{nl} + n_e\alpha^{(r')}_{nl} + n_e\alpha^{(d')}_{nl} + n_e^2\alpha^{(3')}_{nl}$$
$$+ \sum_{nl\neq ml'}\left(A_{nl\to ml'} + n_e q^e_{nl\to ml'} + n_i q^i_{nl\to ml'}\right)\Big\} f_{nl} + \left[n_e\alpha^{(r)}_{nl} + n_e\alpha^{(d)}_{nl} + n_e^2\alpha^{(3)}_{nl}\right] f_i(\boldsymbol{v}-\boldsymbol{V}_r)$$
$$+ \sum_k n_{b_k}|\boldsymbol{v}-\boldsymbol{v}_{b_k}|\sigma^{CX}_{nl}\left(|\boldsymbol{v}-\boldsymbol{v}_{b_k}|\right) f_i(\boldsymbol{v}-\boldsymbol{V}_r), \tag{2}$$

where $f_{nl}(\boldsymbol{r}, \boldsymbol{v}, t)$ represents the ion distribution function with ion charge Z_i after a charge-exchange event, n_e is the free electron density, n_i is the free ion density (that may include both main and impurity ions), $f_i(\boldsymbol{v}-\boldsymbol{V}_r)$ is the shifted distribution function for the charge-exchange receiving impurity ion from Equation (1). The magnetic field $\boldsymbol{B}$ is obtained from the NSTX

EFIT equilibrium reconstruction,[9] and the electric field is calculated using $\boldsymbol{E} = \nabla P_i/(Z+1)en_i - \boldsymbol{V}_r \times \boldsymbol{B}$. The ion pressure is given by $P_i = k_B n_i T_i$. The neutral beam distribution function is represented by $f_b(\boldsymbol{v}') = \sum_k n_{b_k}\delta^3(\boldsymbol{v}' - \boldsymbol{v}_{b_k})$, where n_{b_k} is the density of neutral deuterium for the k^{th} energy component of the beam (for beams with more than one energy component), and $\boldsymbol{v}_{b_k}$ is the k^{th} velocity component of the beam. The calculation of the n_{b_k} densities is explained in detail in Section III. The velocity dependent cross-section for the charge-exchange process into the nl-term is represented by σ_{nl}^{CX}. The kinetic calculation employs measured plasma quantities such as electron temperatures and densities from Multi-Point Thomson Scattering (MPTS), as well as carbon ion densities, temperatures, and plasma rotation from CHERS. Notice that the same kinetic formalism can be applied for an nlj-level resolved representation.

The full solutions for both the nl-term ion density and apparent velocity after a charge-exchange event are[4]

$$
\begin{aligned}
n_{nl}(\boldsymbol{V}_r) &= -n_i \sum_{k=1}^{3}\sum_{\gamma=1}^{N} V_{nl,\gamma}\frac{1}{\lambda_\gamma}\Gamma_\gamma^k(\boldsymbol{V}_r)\\
\boldsymbol{v}_{nl}^{app}(\boldsymbol{V}_r) &= \boldsymbol{V}_r + \frac{\sum_{k=1}^{3}\frac{(\boldsymbol{v}_{b_k}-\boldsymbol{V}_r)}{|\boldsymbol{v}_{b_k}-\boldsymbol{V}_r|}\sum_{\gamma=1}^{N} V_{nl,\gamma}\frac{1}{\lambda_\gamma}\Phi_\gamma^k(\boldsymbol{V}_r)}{\sum_{k=1}^{3}\sum_{\gamma=1}^{N} V_{nl,\gamma}\frac{1}{\lambda_\gamma}\Gamma_\gamma^k(\boldsymbol{V}_r)} + \frac{(\boldsymbol{E}+\boldsymbol{V}_r\times\boldsymbol{B})}{B}\frac{\sum_{k=1}^{3}\sum_{\gamma=1}^{N} V_{nl,\gamma}\frac{1}{\lambda_\gamma}\frac{\frac{\omega_c}{\lambda_\gamma}}{\left(1+\frac{\omega_c^2}{\lambda_\gamma^2}\right)}\Gamma_\gamma^k(\boldsymbol{V}_r)}{\sum_{k=1}^{3}\sum_{\gamma=1}^{N} V_{nl,\gamma}\frac{1}{\lambda_\gamma}\Gamma_\gamma^k(\boldsymbol{V}_r)}\\
&\quad - \frac{\sum_{k=1}^{3}\frac{\boldsymbol{B}}{B}\times\frac{(\boldsymbol{v}_{b_k}-\boldsymbol{V}_r)}{|\boldsymbol{v}_{b_k}-\boldsymbol{V}_r|}\sum_{\gamma=1}^{N} V_{nl,\gamma}\frac{1}{\lambda_\gamma}\frac{\frac{\omega_c}{\lambda_\gamma}}{\left(1+\frac{\omega_c^2}{\lambda_\gamma^2}\right)}\Phi_\gamma^k(\boldsymbol{V}_r)}{\sum_{k=1}^{3}\sum_{\gamma=1}^{N} V_{nl,\gamma}\frac{1}{\lambda_\gamma}\Gamma_\gamma^k(\boldsymbol{V}_r)} + \frac{(\boldsymbol{E}+\boldsymbol{V}_r\times\boldsymbol{B})\times\boldsymbol{B}}{B^2}\frac{\sum_{k=1}^{3}\sum_{\gamma=1}^{N} V_{nl,\gamma}\frac{1}{\lambda_\gamma}\frac{\frac{\omega_c^2}{\lambda_\gamma^2}}{\left(1+\frac{\omega_c^2}{\lambda_\gamma^2}\right)}\Gamma_\gamma^k(\boldsymbol{V}_r)}{\sum_{k=1}^{3}\sum_{\gamma=1}^{N} V_{nl,\gamma}\frac{1}{\lambda_\gamma}\Gamma_\gamma^k(\boldsymbol{V}_r)}\\
&\quad + \frac{\sum_{k=1}^{3}\frac{\boldsymbol{B}\times[\boldsymbol{B}\times(\boldsymbol{v}_{b_k}-\boldsymbol{V}_r)]}{B^2|\boldsymbol{v}_{b_k}-\boldsymbol{V}_r|}\sum_{\gamma=1}^{N} V_{nl,\gamma}\frac{1}{\lambda_\gamma}\frac{\frac{\omega_c^2}{\lambda_\gamma^2}}{\left(1+\frac{\omega_c^2}{\lambda_\gamma^2}\right)}\Phi_\gamma^k(\boldsymbol{V}_r)}{\sum_{k=1}^{3}\sum_{\gamma=1}^{N} V_{nl,\gamma}\frac{1}{\lambda_\gamma}\Gamma_\gamma^k(\boldsymbol{V}_r)},
\end{aligned}
\tag{3}
$$

where λ_γ and $V_{nl,\gamma}$ are the eigen-values and eigen-vectors of the collisional radiative matrix,[4] and the ion gyro-frequency is given by $\omega_c = \frac{Z_i e}{m_i}B$.

The nl-term density population n_{nl} and apparent velocity $\boldsymbol{v}_{nl}$ are used to calculate the line intensities and the Doppler shifted wavelengths due to plasma rotation and atomic physics effects.[4]

A numerical solution using Gauss-Legendre (GL) quadrature is implemented to calculate the quantities Γ_γ^k and Φ_γ^k, which can be written as[4]

$$
\begin{aligned}
\Gamma_\gamma^k(\boldsymbol{V}_r) &= \frac{1}{\sqrt{\pi}}\sum_{i=1}^{\beta} w_{i_k}\left[1+\frac{v_{th}}{|\boldsymbol{v}_{b_k}-\boldsymbol{V}_r|}x_{i_k}\right]e^{-x_{i_k}^2}\sum_{\iota=1}^{N} V_{\gamma,\iota}^{-1}Q_\iota^k(x_{i_k}),\\
\Phi_\gamma^k(\boldsymbol{V}_r) &= \frac{v_{th}}{2\sqrt{\pi}}\sum_{i=1}^{\beta} w_{i_k}\left[1+\frac{v_{th}}{|\boldsymbol{v}_{b_k}-\boldsymbol{V}_r|}x_{i_k}\right]\left[\frac{v_{th}}{|\boldsymbol{v}_{b_k}-\boldsymbol{V}_r|}-2x_{i_k}\right]e^{-x_{i_k}^2}\sum_{\iota=1}^{N} V_{\gamma,\iota}^{-1}Q_\iota^k(x_{i_k}),
\end{aligned}
\tag{4}
$$

where the generalized recombination element as a function of the non-dimensional quantity ν_k is given by

$$
Q_\iota^k(\nu_k) = \frac{1}{3}\left[n_e\alpha_\iota^{(r)} + n_e\alpha_\iota^{(d)} + n_e^2\alpha_\iota^{(3)}\right] + n_{b_k}v_{th}\left|\nu_k + \frac{|\boldsymbol{v}_{b_k}-\boldsymbol{V}_r|}{v_{th}}\right|\sigma_\iota^{CX}\left(\left|v_{th}\left[\nu_k + \frac{|\boldsymbol{v}_{b_k}-\boldsymbol{V}_r|}{v_{th}}\right]\right|\right). \tag{5}
$$

The non-dimensional limits of the quantity ν_k are related to the charge-exchange cross-section upper and lower energy limits,[4] and the quantities x_{i_k} and w_{i_k} are the Gauss-Legendre abscissas and weights of the numerical integration.[10] The full numerical treatment of the solution is explained in detail in Ref. 4.

The line emissivity for a specific $nl \rightarrow ml'$ transition [in units of (Photons/cm^3 s sr)] as a function of plasma parameters at location $\boldsymbol{r}$ is given by

$$\varepsilon_{nl\rightarrow ml'}(\boldsymbol{r}) = \frac{1}{4\pi} A_{nl\rightarrow ml'} n_{nl}(\boldsymbol{r}), \tag{6}$$

where $n_{nl}(\boldsymbol{r})$ is the density population for the nl-term obtained from Equation (3). $A_{nl\rightarrow ml'}$ is the Einstein coefficient for the $nl \rightarrow ml'$ transition with the wavelength $\lambda_{nl\rightarrow ml'}$. From this equation, the full spectra for different ion impurities are calculated.

III. BEAM DENSITIES AND BEAM POPULATION MODELING

Some of the most important quantities in the model are the neutral beam density components n_{b_k} [Equations (2) and (5)], and the n-shell excited population of the deuterons in the neutral beam that donate their electrons to the impurity ions in the plasma through the charge-exchange process.

The neutral beam 1 (NB1) employed on NSTX (and NSTX-U) consists of a bundle of three separate powered sources (or three overlapped beams) named: A, B, and C, each one of them capable of providing a maximum power of 2 MW (a total of 6 MW maximum NB1 power).[11] The typical neutral beam energies for each source are: 45.0, 22.5, and 15 keV/amu for the full, half, and third deuteron energy components.[4] The total neutral beam densities are determined from the measured injected power ($P_{inj} = 2-6$ MW) and the beam acceleration grid bias voltage E_{bias}.[12] The total densities are spatially distributed on the plane perpendicular to the propagation axis, and this spatial distribution is typically measured experimentally.[13] The normalized spatial distribution function is represented by $f(x, y, z)$, where z represents the beam propagation axis, and x and y represent the horizontal and vertical perpendicular distances measured from the beam propagation axis. The normalized spatial distribution function is characteristic of the neutral beam and is independent of plasma parameters or the machine where it operates. The normalized distribution function of NB1 was determined from direct Doppler-shifted Balmer-α line emission measurements on the Tokamak Fusion Test Reactor (TFTR),[13] and it was found that it can be well described by a Lorentzian function (see Figure 2) with horizontal and vertical half widths $w_h = 6.08$ cm and $w_v = 21.79$ cm.

Having the injected beam power, the bias voltage, and the normalized spatial profile, the 3D neutral beam densities can be calculated with[12]

$$n_{b_k}(x,y,z) = \varphi_k \Delta_k(z) \frac{P_{inj}}{\pi e E_{bias} v_{b_k} w_h w_v} f(x,y,z), \tag{7}$$

where the beam attenuation factor as a function of the distance of penetration z for the k^{th} energy component is given by $\Delta_k(z)$, and it is a function of plasma conditions. φ_k represents the beam power fractions for the k^{th}-energy component. The deuterium beam velocities are represented by v_{b_k} for the full ($v_{b_1} = \sqrt{2eE_{bias}/m_D}$), half ($v_{b_2} = \sqrt{eE_{bias}/m_D}$), and third ($v_{b_3} = \sqrt{2eE_{bias}/3m_D}$) energy components, where m_D represents the mass of deuterium. The neutral beam n-shell excited population of the deuterons and beam attenuation depend on their interactions with the hot electrons and ions in the plasma, and are calculated using the time-dependent "hnbeam" code.[4,6] Only interactions with electrons, main ion, and main impurity (plasma deuterons and fully stripped carbon) are taken into account in the beam calculation since these quantities are already available from MPTS and CHERS measurements. The "hnbeam" is a time-dependent code based on an analytic solution[6] of the bundle-$n = 5$ atomic populations of the deuterium beam. The solution for each of the 5 n-shell populations [$n_n(z)$] as a function of beam propagation distance z is calculated for an arbitrarily small grid step $z - z_o$ (depending on the electron/ion temperature and density gradients along the beam propagation direction) and is given by

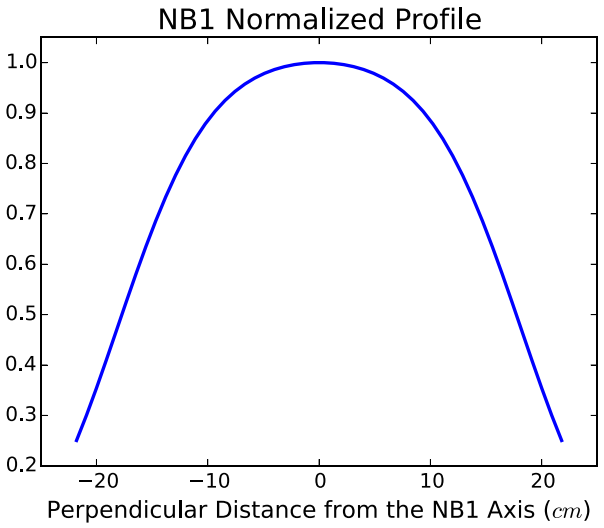

FIG. 2. The NB1 normalized spatial profile is well described using a Lorentzian function that fits measurements from Doppler-shifted Balmer-α line emission on TFTR.[13] NB1 operated on TFTR before being transferred to NSTX.

$$n_n(z) = \sum_{l=1}^{N} V_{n,l}(z) \sum_{m=1}^{N} V_{l,m}^{-1}(z) n_m(z_o) e^{\lambda_l(z)\frac{z-z_o}{v_b}}. \tag{8}$$

Here, v_b represents the magnitude of the beam propagation velocity, $V_{n,l}(z)$ are the eigenvector elements of the collisional radiative matrix [with its inverse $V_{l,m}^{-1}(z)$], and $\lambda_l(z)$ are the eigenvalues of the matrix calculated for the local plasma parameters at the z location along the beam propagation axis.[4,6] The initial position is represented by z_o, and the calculation is done in small step intervals represented by $z - z_o$. This beam model includes bundle-n electron/ion impact ionization, as well as excitation/de-excitation, and charge-exchange with deuterons and fully stripped carbon ions, while electron-impact ionization and excitation/de-excitation rate coefficients are assumed to be Maxwellian. The rate coefficients for ion-impact are calculated taking into account the local plasma parameters and a shifted Maxwellian distribution [Equation (1)], with the non-dimensional quantity ν_k are calculated using

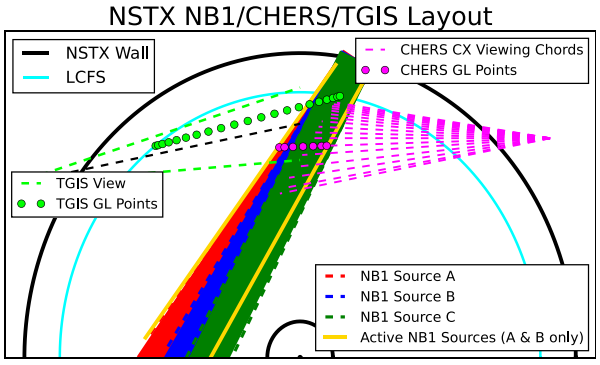

FIG. 3. The general layout of the NB1 together with the TGIS diagnostic spatial view and a single CHERS spectral viewing chord on NSTX are shown in this figure. The NB1 consists of three independently operated power sources (sources A, B, and C) with a contribution of 2 MW each (6 MW total NB1 power). The CHERS diagnostic spectral viewing chords as well as the TGIS view cross the NB1 3-D profile to detect beam into plasma impurity charge-exchange emission. To model the emission for both CHERS and TGIS, the numerical integration along the line-of-sight is calculated using GL numerical integration quadrature.[10] The region of integration for modeling charge-exchange is limited to the "powered" volume of NB1, which varies with respect to the active powered sources. For calculating the Bremsstrahlung continuum emission for the TGIS, the integration region is limited to the volume inside the Last Closed Flux Surface (LCFS). For the shot analyzed in this work (NSTX shot 142192), only the A and B power sources were active. This figure shows the boundaries of the active sources that define the limits of the Gauss-Legendre numerical integration for CHERS.

$$q_n(\boldsymbol{v}_{b_k},\boldsymbol{V}_r)=\frac{1}{\pi^{3/2}v_{th}^3}\int d^3\boldsymbol{v}|\boldsymbol{v}-\boldsymbol{v}_{b_k}|\sigma_n(\boldsymbol{v}-\boldsymbol{v}_{b_k})e^{-(\boldsymbol{v}-\boldsymbol{V}_r)^2/v_{th}^2}$$
$$=\frac{1}{\sqrt{\pi}}\frac{v_{th}^2}{|\boldsymbol{v}_{b_k}-\boldsymbol{V}_r|}\int_{-\infty}^{\infty}d\nu_k\left[\nu_k+\frac{|\boldsymbol{v}_{b_k}-\boldsymbol{V}_r|}{v_{th}}\right]^2\sigma_n(\nu_k)e^{-\nu_k^2}, \quad (9)$$

where the rate coefficient is also a function of the local impurity ion rotation velocity $\boldsymbol{V}_r$. Ion impurity rotation may become important when the magnitude of $\boldsymbol{V}_r$ becomes comparable to the neutral beam propagation velocities $\boldsymbol{v}_{b_k}$.[14] The "hnbeam" time-dependent code retains the capability of including impurity ion rotation velocities and is numerically efficient when calculating the ion-impact rate coefficients directly from cross-sections, thus eliminating the need of pre-calculated tables of beam stopping coefficients used by other beam codes.[15,16] Figure 4(c) shows the attenuation radial profile $[n_{b_k}(r)]$ for the three energy components of NB1 on NSTX shot 142192 ($t=0.815$ s).

IV. ATOMIC DATA

Most of the atomic data included in the kinetic model was obtained from the Atomic Data and Analysis Structure (ADAS) database.[17] The atomic data for hydrogen-like carbon consist of state-of-the-art electron-impact excitation data calculated using the R-Matrix with Pseudostates (RMPS) method combined with plane-wave-Born (PWB) data,[18,19] and are described in detail by Ballance *et al.*[20] The bundle-nl electron-impact excitation data include transitions between the same n-shell ($nl \rightarrow nl'$). The Einstein A-coefficients were calculated for a maximum value of $n=17$ shell for hydrogen-like carbon using the AUTOSTRUCTURE atomic code.[21] The atomic data for chlorine, iron, and copper ions includes PWB and Distorted-Wave (DW) electron excitation. For all impurities, the electron-impact ionization rate coefficients were calculated by the Exchange Classical Impact Parameter (ECIP) method,[22] which have been found to be accurate when compared to those calculated from non-perturbative methods.[23] The radiative recombination coefficients were calculated by using the Cowan atomic structure code,[24,25] while the 3-body recombination coefficients were obtained by detailed balance[26] from the ECIP ionization data by means of the "r8necip" ADAS subroutine.[17,27] The ion-impact excitation rate coefficients were calculated by impact parameter using the "rpengv" ADAS subroutine,[17] and the ion-impact ionization rate coefficients were calculated using the Percival and Richards expression by means of the "rqinew" ADAS subroutine.[17,28]

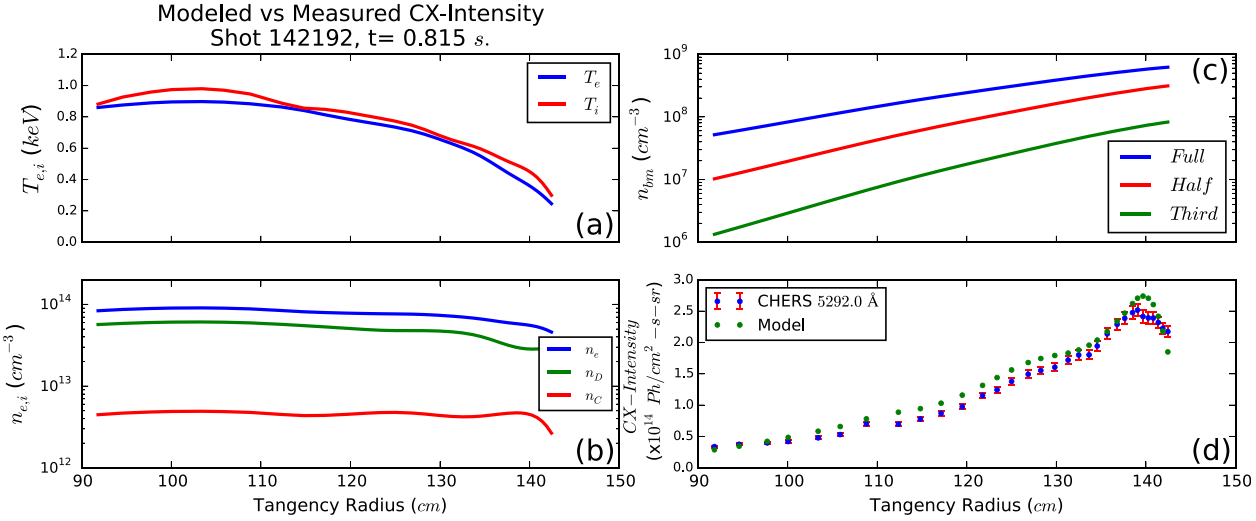

FIG. 4. Comparison between the modeled and measured (CHERS $\lambda=5292.0$ Å line) charge-exchange emission profiles for NSTX shot 142192 (d). (a) and (b) Measured electron and ion temperature and density radial profiles from MPTS and CHERS. These profiles are used to calculate the NB1 plasma penetration for the full, half, and third energy components shown in (c). The measured electron/ion temperature, density, and radial NB1 profiles are also used in the kinetic emission calculation of the line-of-sight integrated charge-exchange intensity profile shown in (d).

The charge-exchange data for carbon include *nl*-term resolved cross-sections that include up to the $n=17$ shell from the ADAS database.[17] These cross-sections also include charge-exchange from the $n=1\rightarrow 4$ excited populations of deuterium in the neutral beam, and the total *n*-resolved cross-sections of carbon are distributed to each of the *nl*-terms using

$$\sigma_{nl}^{CX}=\frac{\sqrt{l+1}}{\sum_{l'=0}^{n-1}\sqrt{l'+1}}\sigma_{n}^{CX}, \tag{10}$$

where the quantum states with the highest angular momentum l ($l\approx n-1$) are preferred during the charge-exchange process.[29]

For all other ion impurities included in this work, the charge-exchange cross-sections were approximated by semi-classical treatment from Hutchinson.[29] This semi-classical approach has shown agreement with various full calculations of charge-exchange cross-sections.[29] The different *nlj*-levels are populated from the neutral beam by splitting the cross-sections assuming statistical distributions. To predict accurate wavelengths in the spectra, the values of the energy levels of the ions were replaced by those from NIST.[30]

V. BENCHMARK OF THE KINETIC MODEL WITH CHERS

To assure that the kinetic model produces reasonable emission results, predictions are first compared to absolute calibrated line-integrated emission from the C VI ($n=8\rightarrow 7$) visible line ($\lambda=5292.0$ Å) measured by CHERS.

Figure 3 shows the geometry of the NB1 on NSTX crossing a single CHERS spectral viewing chord. It also shows the location and spatial view of the TGIS diagnostic that intercepts the neutral beam near the edge of the plasma. The neutral beam (NB1) consists of three sources (A, B, and C) that can be powered independently and that overlap with each other along the central beam propagation axis.

For the NSTX shot analyzed in this work (142192), only NB1 sources A and B were powered; therefore, the line-of-sight GL numerical integration[10] for the charge-exchange calculation is limited to the volume enclosed by the sources A and B (Figure 3). The charge-exchange emission is calculated for both CHERS and TGIS diagnostics. It was determined that a minimum of 5 Gauss-Legendre integration points along the NB1 active region are sufficient to obtain convergence. Gauss-Legendre numerical integration along the line-of-sight is also used to model Bremsstrahlung emission detected by the TGIS diagnostic. In this case, the integration is performed along the entire volume of the plasma inside the Last Closed Flux Surface (LCFS, Figure 3). The reason for this limitation is due to the square of the electron density dependence (n_e^2) of the Bremsstrahlung continuum emission [Equation (13)] detected by the TGIS, and which falls over two orders of magnitude outside the LCFS.

Figure 4(d) shows the comparison between the modeled and measured $\lambda=5292.0$ Å charge-exchange line intensities for all of the 32 CHERS spectral viewing chords looking to the core of NSTX. Measured electron/ion temperature (a) and density (b) radial profiles together with calculated neutral beam attenuation densities (c) (for the three neutral beam energy components) employed by the kinetic calculation are also shown.

In general, the kinetic model predicts slightly higher emission than the CHERS measurements, especially in the edge region, as shown in Figure 4(d). There are two known effects that may explain these discrepancies: First, the CHERS diagnostic employs the ADAS beam model[17] that only includes up to the $n=2$ excited population of the neutral beam to charge-exchange with the fully stripped carbon ions. It has been suggested that higher *n*-shell populations in the neutral beam must be included in order to account for emission from higher C VI transitions.[31] The kinetic model includes charge-exchange from the $n=1\rightarrow 4$ excited populations of deuterium in the neutral beam (Section IV). The second source of discrepancy may be attributed to additional emission from carbon due to charge-exchange with halo neutrals produced by the beam.[32,33] A recent 3-D halo neutral code developed at the Princeton Plasma Physics Laboratory and implemented for analysis using the TRANSP code predicts halo neutral densities ~25% greater than the beam neutrals, particularly at the plasma edge.[34] The halo neutrals remain in the vicinity of the neutral beam footprint[34] and can also undergo charge-exchange with carbon thus increasing the emission of the $\lambda=5292.0$ Å line. The model employed to determine carbon densities from CHERS does not take into account halo contributions to the emission; therefore, it is possible that the derived densities may be overestimated, particularly around the edge. The kinetic model uses derived carbon densities from CHERS to calculate charge-exchange emission profiles. If the CHERS densities are overestimated due to halo contributions, it is expected that the kinetic model will predict slightly higher emission profiles, particularly at the edge, as shown in Figure 4(d).

The kinetic model is also capable to predict other transitions, such as Lyman (transitions to $n=1$), Balmer (to $n=2$), Paschen (to $n=3$), and Brackett (to $n=4$), up to the $n=16$ transition series for hydrogen-like carbon. These calculations include the most intense lines in order to predict a full C VI charge-exchange spectra.

Figure 5 shows a complete modeled C VI spectrum integrated along the 9th CHERS spectral viewing chord ($R_{Tan}\approx 122.0$ cm) for NSTX shot 142192.

VI. BREMSSTRAHLUNG EMISSION CALIBRATION AND QUANTIFICATION OF IMPURITY DENSITIES

Absolute intensity calibration (or recalibration) of XUV spectrometers using Bremsstrahlung continuum emission offers many advantages.[7] Bremsstrahlung emission spectra peaks around the XUV region, it varies inversely with respect to wavelength and directly proportional to both Z_{eff} and the square of electron density [Equation (13)]. Due to the typical electron densities present in the core and edge regions of tokamak plasmas ($n_e\geq 10^{14}\,\mathrm{cm}^{-3}$), strong Bremsstrahlung emission is expected in the XUV spectral region inside the volume limited by the LCFS.

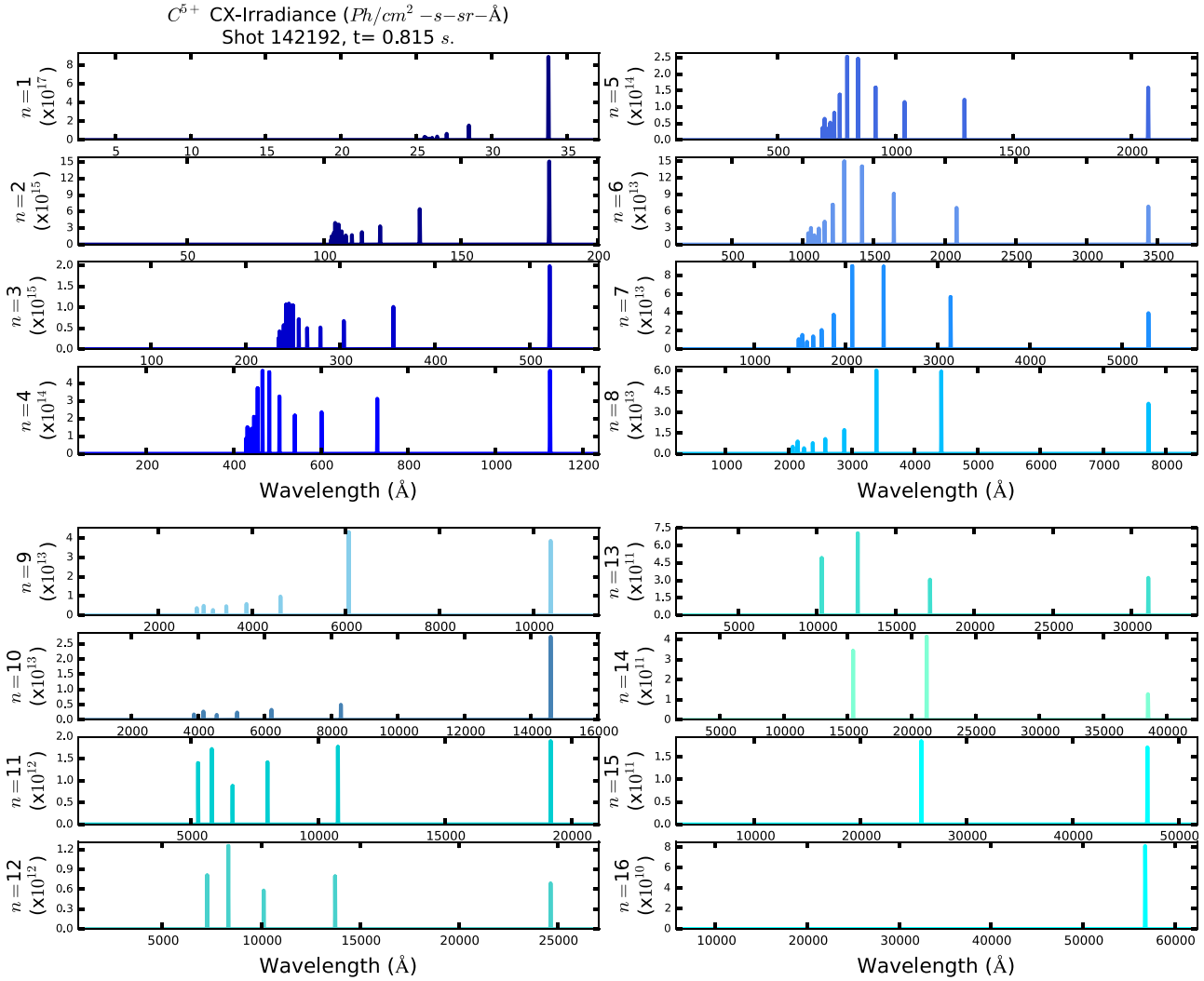

FIG. 5. Modeled C^{5+} CX-spectra integrated along the 9th spectral viewing chord ($R_{Tan} \approx 122.0$ cm) of CHERS. The spectra are shown with respect to its lowest transition n-shell, such as Lyman (transitions to $n=1$), Balmer (to $n=2$), and Paschen (to $n=3$), etc., of hydrogen-like carbon. The wavelengths in the spectra include shifts due to plasma rotation and atomic physics effects.[4]

In previous work,[7] precise absolute intensity calibration of a space-resolved XUV spectrometer was carried out using scaled Bremsstrahlung emission in a large helical device. The free-free Bremsstrahlung continuum emission measured in the XUV was scaled to absolute intensity calibrated Bremsstrahlung measurements in the visible. From this scaling, an absolute calibration curve was obtained.[7] On NSTX, Bremsstrahlung continuum emission in the visible is measured only with a single spectral chord, and a flat profile is assumed in the interpretation of the data. An accurate scaling of the XUV Bremsstrahlung with respect to the visible for calibration purposes is not currently possible; therefore, the kinetic charge-exchange model is employed to estimate the scaling.

In this work, the charge-exchange 181.1 Å line of C VI calculated using the kinetic model is used as a reference to scale the Bremsstrahlung continuum emission in the XUV. The $\lambda = 181.1$ Å line was chosen due to its strong emission relative to the Bremsstrahlung continuum, and its relative isolation from other impurity lines in the XUV, as shown in Figure 7(b). The scaled Bremsstrahlung emission is then used to estimate an absolute calibration curve for the TGIS.

The total Bremsstrahlung continuum radiation includes both free-free and recombination contributions to the lowest unfilled n-shell. The emissivity as a function of wavelength (λ) can be written as[29]

$$\varepsilon_{Bremm}^{Total}(\lambda) = \sum_i n_e n_i Z_i^2 \left(\frac{e^2}{4\pi\varepsilon_o}\right)^3 \frac{8\pi\times 10^6}{3m_e^2 hc^3}\sqrt{\frac{2m_e}{3e\pi}}\frac{1}{\sqrt{T_e}\lambda} \times e^{-ehc/T_e\lambda}\left[\bar{g}_{ff} + G_n \frac{\xi}{n^5}\frac{Z_i^2 R_y}{T_e} e^{Z_i^2 R_y/n^2 T_e} + \sum_{\upsilon=n+1}^{\infty} G_\upsilon \frac{Z_i^2 R_y}{\upsilon^2 T_e}\frac{2\lambda}{c} e^{Z_i^2 R_y/\upsilon^2 T_e}\right] \left(\mathrm{ph/cm^3 - s - sr - Å}\right), \quad (11)$$

where the sum is performed for each of the ion charges and densities (Z_i and n_i), T_e and n_e represent the local electron temperature and density (in units of eV and cm^{-3}), and λ represents the wavelength in Å. The quantities $\bar{g}_{ff}$ and G_n are the gaunt factors for both the free-

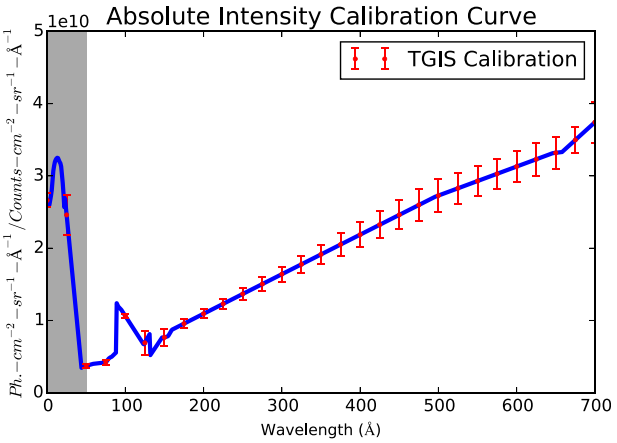

FIG. 6. TGIS absolute intensity calibration curve estimated from scaled Bremsstrahlung continuum emission. The TGIS XUV sensitivity ranges from ∽50 to 700 Å. The shaded area ($\lambda < 50$ Å) represents the "blind" region of the detector.

free and recombination contributions, which are function of the local electron temperature, photon energy, and Z_{eff}. The gaunt factors are calculated using the "r8gbf" and "r8gav" ADAS subroutines.[17] As shown in Figure 7(a,V), the recombination contributions to the Bremsstrahlung become important for wavelengths $\lambda < 50$ Å. The TGIS diagnostic is insensitive for wavelengths below 50 Å; therefore, only the free-free contribution is considered when calibrating the TGIS.

Without the recombination contributions, the sum over the ion charges and densities (Z_i and n_i) in Equation (11) can be written in terms of Z_{eff} using

$$n_e^2 Z_{eff} = \sum_i n_e n_i Z_i^2 . \tag{12}$$

Equation (11) is reduced to

$$\varepsilon_{Bremm}^{free-free}(\lambda) = n_e^2 Z_{eff} \left(\frac{e^2}{4\pi\varepsilon_o}\right)^3 \times \frac{8\pi \times 10^6}{3m_e^2 hc^3} \sqrt{\frac{2m_e}{3e\pi}} \frac{\bar{g}_{ff}}{\sqrt{T_e}\lambda} e^{-ehc/T_e\lambda} . \tag{13}$$

The TGIS diagnostic consists on an entrance slit, and imaging slit (grating), and a CsI coated micro-channel plate (MCP)[35] as a 2-D detector to resolve radial and spectral simultaneous measurements.[1]

In this work, the ratio between the 181.1 Å line and the Bremsstrahlung continuum emission at the same wavelength region is obtained from the measured TGIS spectra [Figure 7(b)]. This ratio is then used as a reference to scale the modeled Bremsstrahlung calculated using Equation (13) with respect to the absolute 181.1 Å line intensity obtained from the kinetic model. The confidence of the absolute intensity value of the 181.1 Å line is based on the agreement between CHERS measurements and absolute intensity values calculated using the kinetic model for the $\lambda = 5292.0$ Å line [Figure 4(d)].

The modeled Bremsstrahlung emission requires knowledge of Z_{eff} [Equation (13)], which depends on the sum of all impurity densities in the plasma. The main impurity present on NSTX is carbon, and its density, temperature, and rotation velocity values are measured using the CHERS diagnostic. The electron temperatures and densities are obtained from MPTS. Therefore, as a first approximation, a partial Z_{eff} that only includes deuterium and carbon is calculated using the CHERS and MPTS measurements. The partial Z_{eff} is used to estimate an absolute intensity calibration curve for the TGIS to determine impurity densities.

Using the obtained impurity densities, a total Z_{eff} is calculated and used to model the scaled Bremsstrahlung emission to recalibrate the TGIS to obtain a new set of impurity densities. It was found that the total Z_{eff} differs from the partial one by <2.5% [see Figure 8(b)]. It is therefore concluded

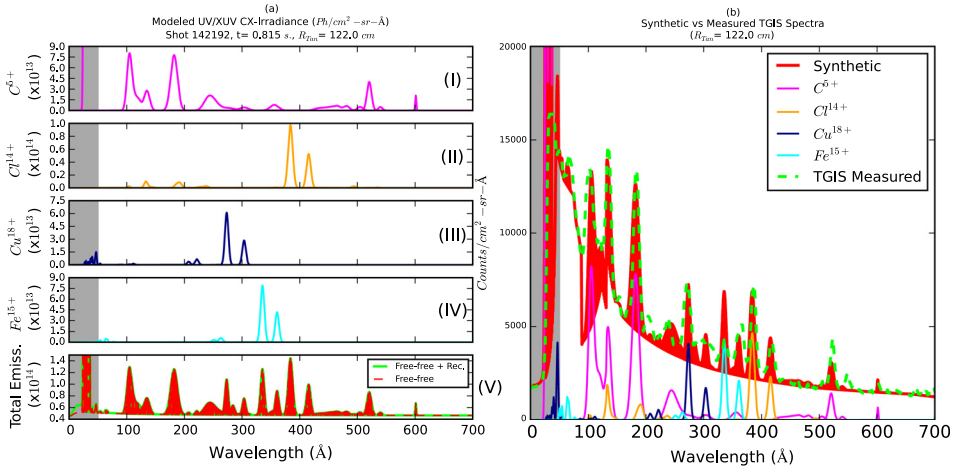

FIG. 7. Modeled irradiance and synthetic TGIS spectra for the radial location $R_{Tan} = 122.0$. (a) The modeled XUV charge-exchange spectra for the main impurity ion C^{5+} (I), as well as other observed impurities [Cl^{14+} (II), Cu^{18+} (III), and Fe^{15+} (IV)]. The total spectra consist of the addition of both the charge-exchange and modeled Bremsstrahlung continuum emission as shown in (V). The modeled Bremsstrahlung includes free-free, as well as total (free-free + recombination) contributions. The shaded wavelength window ($\lambda < 50$ Å) represents the insensitive ("blind") region of the TGIS detector. It is noticed that for wavelengths $\lambda > 50$ Å, both the free-free and the total (free-free + recombination) Bremsstrahlung agree with each other. It is therefore concluded that the free-free contribution to the modeled Bremsstrahlung [Equation (13)] is sufficient to estimate the absolute intensity calibration curve of the TGIS diagnostic.[7] (b) Comparison between the synthetic and measured TGIS spectra. The synthetic spectra are calculated by convolving the modeled irradiance with the inverse of the absolute calibration curve (Figure 6), and by varying the Cl^{15+}, Cu^{19+}, and Fe^{16+} impurity ion densities to fit the measured TGIS spectra.

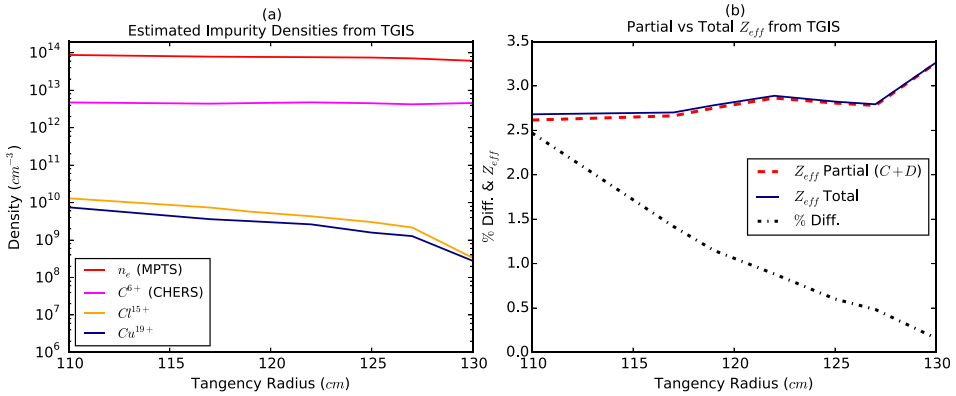

FIG. 8. Quantified impurity densities and Z_{eff} radial profiles derived from the TGIS diagnostic on NSTX. (a) The impurity ion densities estimated by fitting synthetic emission to TGIS spectra. The electron and carbon densities are also shown as points of comparison. The main impurity ion (C^{5+}) is obtained from the CHERS diagnostic, while electron densities are obtained from MPTS. (b) The partial and total Z_{eff} radial profiles. The partial Z_{eff} includes only the contributions of carbon and deuterium (obtained from CHERS and MPTS), while the total Z_{eff} is calculated using all the quantified impurities. The %-difference between the two is also shown in the figure. It is noticed that the contributions from the measured impurity densities to the total Z_{eff} is below 2.5%, thus justifying the use of the partial Z_{eff} for Bremsstrahlung-based initial calibration of the TGIS diagnostic. It is also noticed that although the impurity densities decrease with respect to tangency radius, the Z_{eff} increases. This is explained by the slight decrease in electron density shown in (a) [see also Figure 4(b)].

that a partial Z_{eff} dominated by deuterium and carbon is sufficient when modeling Bremsstrahlung emission for calibration purposes. This assumption may be better applied when high electron densities and low impurity content are present in the plasma core such as during elming H-mode plasma regimes.

The scaled Bremsstrahlung continuum emission detected by the TGIS is calculated by numerically integrating the emissivities [Equation (13)] along the line-of-sight of the spectral viewing chord through the plasma volume enclosed by the LCFS (Figure 3) using Gauss-Legendre quadrature.[10] The impurity emission from charge-exchange detected by the TGIS is obtained from integration along the line-of-sight of the NB1 active region as in the case of CHERS (Figure 3).

In order to calibrate the TGIS with respect to the scaled Bremsstrahlung continuum emission, several spectral "windows" of absent charge-exchange emission are chosen such as: $74.2 \rightarrow 89.0$, $123.5 \rightarrow 123.7$, $147.0 \rightarrow 160.0$, $216.2 \rightarrow 216.8$,…, $657.5 \rightarrow 658.0$ Å [see Figure 7(b)]. The calculation is performed for different radial locations of the TGIS, several absolute intensity calibration curves are obtained from these radial locations, and the final calibration function of the instrument is calculated by averaging all of the curves. The estimated uncertainties on the final calibration are obtained from the standard deviation. A source of uncertainty when measuring spectra from different radial locations comes from the angular sensitivity of the CsI coated 2-D detector.[35] These variations are intrinsically included in the calculated uncertainties. Figure 6 shows the final TGIS absolute intensity calibration curve obtained from the scaled Bremsstrahlung continuum emission.

The calibration curve shows a pronounced spike between $0 \rightarrow 50$ Å. This "blind" region represents a loss of sensitivity of the CsI coated MCP detector for such low wavelengths.[35] In this wavelength region, the recombination contributions to the Bremsstrahlung continuum emission become important [Figure 7(a,V)].

The total modeled spectra are calculated by adding the scaled Bremsstrahlung continuum emission, and the beam charge-exchange spectra for different impurity ions predicted by the kinetic model at different TGIS radial locations. A synthetic spectrum is produced by convolving the modeled spectra with the inverse of the absolute intensity calibration curve, and an instrumental line width is artificially added. The impurity densities are determined by fitting the synthetic line intensities to the measured TGIS spectra.

Figure 7(a) shows the predicted XUV charge-exchange spectra for the C^{5+}, Cl^{14+}, Cu^{18+}, and Fe^{15+} impurity ions, as well as their sum with the Bremsstrahlung continuum for both the free-free and the total (free-free + recombination) at the TGIS radial location $R_{Tan} = 122.0$. The shaded area represents the insensitive ("blind") region of the TGIS detector ($\lambda < 50$ Å). Figure 7(b) shows the synthetic spectra fitted to the actual TGIS measurements.

Figure 7(a,V) shows the modeled Bremsstrahlung continuum spectra. Notice that the recombination contributions to Bremsstrahlung become important for wavelengths $\lambda < 50$ Å; therefore, the free-free contribution of the Bremsstrahlung emission becomes the main factor to consider for TGIS calibration purposes.[7]

Figure 8(a) shows quantified Cl^{15+} and Cu^{19+} impurity densities compared to main impurity ion (carbon) and electron densities. Figure 8(b) shows the partial and total Z_{eff} radial profiles and their %-difference. It was found that the spectrum was dominated by charge-exchange emission, other ions were also modeled, but only the main contributors were included in the final spectra.

The fitted spectra shown in Figure 7(b) are limited by the quality of the atomic data available for each specific impurity, especially when it comes to charge-exchange cross-sections. This becomes more evident specially when closely examining the synthetic spectra for Fe^{15+}, where the two lines do not fit the measurements [Figure 7(b)].

In this work, the charge-exchange cross-sections for Cl, Cu, and Fe were approximated using a semi-classical approximation from Hutchinson.[29] Even though this semi-classical approach yields cross-sections that agree within a factor of two with various full calculations,[29] the charge-

exchange population distribution split statistically into *nlj*-levels may represent a main source of discrepancies in the fitted spectra. This is difficult to assess due to the complex dependence of charge-exchange cross-sections with respect to angular momentum.[36] There have been efforts made to determine charge-exchange cross-sections from X-ray spectra, but it requires an accurate and efficient calibration of X-ray spectrometers.[37]

VII. CONCLUSIONS

Quantification of plasma impurities from charge-exchange emission spectroscopy can be accomplished using advanced kinetic collisional radiative modeling. Quantitative measurements of impurity profiles will play a key role on NSTX-U, especially when high-*Z* metallic tiles are introduced on the lower divertor.[3] A great deal of emission from metallic impurities occurs in the XUV/VUV region, and eventually, these kinds of measurements will become important to support high-*Z* transport studies during high plasma rotation regimes.

Absolute intensity calibration of XUV spectrometers can also be accomplished using Bremsstrahlung continuum emission that has been scaled with respect to emission predictions from advanced kinetic collisional radiative models, although additional emission due to charge-exchange with halo neutrals may also need to be considered.[32–34] Using this method, an absolute intensity calibration curve was estimated for the TGIS on NSTX. This represents a calibration/recalibration alternative for XUV/VUV spectrometers that may suffer loss of sensitivity due to neutron bombardment, and that absolute calibration using synchrotron sources may be unpractical.

ACKNOWLEDGMENTS

The work at Johns Hopkins University was supported by the U.S. Department of Energy (DoE) under Grant: DE-S0000787. The work at PPPL was supported under U.S. DoE Grant: DE-AC02-09ch11466.

[1]D. Kumar, M. Finkenthal, D. Stutman, R. E. Bell, D. J. Clayton, A. Diallo, B. P. LeBlanc, M. Podesta, and K. Tritz, Plasma Phys. Controlled Fusion **54**, 065010 (2012).
[2]R. Isler, Nucl. Fusion **24**, 1599 (1984).
[3]J. E. Menard, S. Gerhardt, M. Bell, J. Bialek, A. Brooks, J. Canik, J. Chrzanowski, M. Denault, L. Dudek, D. A. Gates, N. Gorelenkov, W. Guttenfelder, R. Hatcher, J. Hosea, R. Kaita, S. Kaye, C. Kessel, E. Kolemen, H. Kugel, R. Maingi, M. Mardenfeld, D. Mueller, B. Nelson, C. Neumeyer, M. Ono, E. Perry, R. Ramakrishnan, R. Raman, Y. Ren, S. Sabbagh, M. Smith, V. Soukhanovskii, T. Stevenson, R. Strykowsky, D. Stutman, G. Taylor, P. Titus, K. Tresemer, K. Tritz, M. Viola, M. Williams, R. Woolley, H. Yuh, H. Zhang, Y. Zhai, A. Zolfaghari, and NSTX Team, Nucl. Fusion **52**, 083015 (2012).
[4]J. M. M. Burgos, K. H. Burrell, W. M. Solomon, B. A. Grierson, S. D. Loch, C. P. Ballance, and C. Chrystal, Nucl. Fusion **53**, 093012 (2013).
[5]K. H. Burrell and J. M. M. Burgos, Phys. Plasmas **19**, 072507 (2012).
[6]J. M. M. Burgos, O. Schmitz, S. D. Loch, and C. P. Ballance, Phys. Plasmas **19**, 012501 (2012).
[7]C. Dong, S. Morita, M. Goto, and E. Wang, Rev. Sci. Instrum. **82**, 113102 (2011).
[8]L. Delgado-Aparicio, D. Stutman, K. Tritz, F. Volpe, K. L. Wong, R. Bell, M. Finkenthal, E. Fredrickson, S. P. Gerhardt, S. Kaye, B. LeBlanc, J. Menard, S. Paul, and L. Roquemore, Nucl. Fusion **51**, 083047 (2011).
[9]S. A. Sabbagh, J. W. Ahn, J. Allain, R. Andre, A. Balbaky, R. Bastasz, D. Battaglia, M. Bell, R. Bell, P. Beiersdorfer, E. Belova, J. Berkery, R. Betti, J. Bialek, T. Bigelow, M. Bitter, J. Boedo, P. Bonoli, A. Boozer, A. Bortolon, D. Boyle, D. Brennan, J. Breslau, R. Buttery, J. Canik, G. Caravelli, C. Chang, N. Crocker, D. Darrow, B. Davis, L. Delgado-Aparicio, A. Diallo, S. Ding, D. D'Ippolito, C. Domier, W. Dorland, S. Ethier, T. Evans, J. Ferron, M. Finkenthal, J. Foley, R. Fonck, R. Frazin, E. Fredrickson, G. Fu, D. Gates, S. Gerhardt, A. Glasser, N. Gorelenkov, T. Gray, Y. Guo, W. Guttenfelder, T. Hahm, R. Harvey, A. Hassanein, W. Heidbrink, K. Hill, Y. Hirooka, E. B. Hooper, J. Hosea, D. Humphreys, K. Indireshkumar, F. Jaeger, T. Jarboe, S. Jardin, M. Jaworski, R. Kaita, J. Kallman, O. Katsuro-Hopkins, S. Kaye, C. Kesse, J. Kim, E. Kolemen, G. Kramer, S. Krasheninnikov, S. Kubota, H. Kuge, R. J. L. Haye, L. Lao, B. LeBlanc, W. Lee, K. Lee, J. Leuer, F. Levinton, Y. Liang, D. Liu, J. Lore, N. Luhmann, Jr., R. Maingi, R. Majeski, J. Manickam, D. Mansfield, R. Maqueda, E. Mazzucato, A. McLean, D. McCune, B. McGeehan, G. McKee, S. Medley, E. Meier, J. Menard, M. Menon, H. Meyer, D. Mikkelsen, G. Miloshevsky, D. Mueller, T. Munsat, J. Myra, B. Nelson, N. Nishino, R. Nygren, M. Ono, T. Osborne, H. Park, J. Park, Y. S. Park, S. Paul, W. Peebles, B. Penaflor, R. J. Perkins, C. Phillips, A. Pigarov, M. Podesta, J. Preinhaelter, R. Raman, Y. Ren, G. Rewoldt, T. Rognlien, P. Ross, C. Rowley, E. Ruskov, D. Russell, D. Ruzic, P. Ryan, M. Schaffer, E. Schuster, F. Scotti, K. Shaing, V. Shevchenko, K. Shinohara, V. Sizyuk, C. H. Skinner, A. Smirnov, D. Smith, P. Snyder, W. Solomon, A. Sontag, V. Soukhanovskii, T. Stoltzfus-Dueck, D. Stotler, B. Stratton, D. Stutman, H. Takahashi, Y. Takase, N. Tamura, X. Tang, G. Taylor, C. Taylor, K. Tritz, D. Tsarouhas, M. Umansky, J. Urban, E. Untergberg, M. Walker, W. Wampler, W. Wang, J. Whaley, R. White, J. Wilgen, R. Wilson, K. L. Wong, J. Wright, Z. Xia, D. Youchison, G. Yu, H. Yuh, L. Zakharov, D. Zemlyanov, G. Zimmer, and S. J. Zweben, Nucl. Fusion **41**, 1601 (2001).
[10]W. H. Press, S. A. Teukolsky, W. T. Vetterling, and B. P. Flannery, *Numerical Recipes the Art of Scientific Computing*, 3rd ed. (Cambridge University Press, New York, 2007).
[11]S. S. Medley, Ya. I. Kolesnichenko, Yu. V. Yakovenko, R. E. Bell, A. Bortolon, N. A. Crocker, D. S. Darrow, A. Diallo, C. W. Domier, R. J. Fonck, E. D. Fredrickson, S. P. Gerhardt, N. N. Gorelenkov, G. J. Kramer, S. Kubota, B. P. LeBlanc, K. C. Lee, E. Mazzucato, G. R. McKee, M. Podest, Y. Ren, A. L. Roquemore, D. R. Smith, D. Stutman, K. Tritz, and R. B. White, Nucl. Fusion **52**, 013014 (2012).
[12]M. G. Von Hellermann and H. P. Summers, in *In Active Beams Spectroscopy at JET: Atomic and Plasma Material Interaction Processes in Controlled Thermonuclear Fusion*, edited by R. K. Janev and H. W. Drawing (Elsevier, Amsterdam and New York, 1993).
[13]J. H. Kamperschroer, L. R. Grisham, N. Kokatnur, L. J. Lagin, and R. A. Newman, Rev. Sci. Instrum. **66**, 130–138 (1995).
[14]R. B. Howell, R. J. Fonck, R. J. Knize, and K. P. Jaehnig, Rev. Sci. Instrum. **59**, 1521 (1988).
[15]I. H. Hutchinson, Plasma Phys. Controlled Fusion **44**, 71–82 (2002).
[16]E. Delabie, M. Brix, C. Giroud, R. J. E. Jasper, O. Marchuk, M. G. O'Mullane, Yu. Ralchenko, E. Surrey, M. G. Von Hellermann, K. D. Zastrow, and JET-EFDA Contributors, Plasma Phys. Controlled Fusion **52**, 125008 (2010).
[17]H. P. Summers, The ADAS User Manual, version 2.6, 2004, see http://www.adas.ac.uk.
[18]P. G. Burke and K. A. Berrington, *Atomic and Molecular Processes: An R-Matrix Approach* (Institute of Publishing (IOP), Bristol, 1993).
[19]K. Bartschat, Comput. Phys. Commun. **114**, 168 (1998).
[20]C. P. Ballance, N. R. Badnell, and E. S. Smyth, J. Phys. B: At., Mol. Opt. Phys. **36**, 3707 (2003).
[21]N. R. Badnell, J. Phys. B: At., Mol. Opt. Phys. **19**, 3827 (1986).
[22]A. Burgess and H. P. Summers, Mon. Not. R. Astron. Soc. **174**, 345 (1976).
[23]S. D. Loch, C. P. Ballance, M. S. Pindzola, and D. P. Stotler, Plasma Phys. Controlled Fusion **51**, 105006 (2009).
[24]R. D. Cowan, *The Theory of Atomic Structure and Spectra* (University of California Press, Berkeley, CA, 1981).
[25]See http://www.tcd.ie/Physics/People/Cormac.McGuinness/Cowan.
[26]Y. Hahn, Rep. Prog. Phys. **60**, 691 (1997).
[27]R. M. Pengelly and M. J. Seaton, Mon. Not. R. Astron. Soc. **127**, 165 (1964).
[28]I. C. Percival and D. Richards, J. Phys. B: At., Mol. Opt. Phys. **3**, 1035 (1970).

[29]I. H. Hutchinson, *Principles of Plasma Diagnostics*, 2nd ed. (Cambridge University Press, Cambridge, UK, 2002).
[30]See http://www.nist.gov.
[31]M. Podesta, R. E. Bell, A. Diallo, B. P. LeBlanc, F. Scotti, and NSTX Team, Nucl. Fusion **52**, 033008 (2012).
[32]R. C. Isler, Phys. Scr. **35**, 650–661 (1987).
[33]T. Ito, M. Osakabe, K. Ida, M. Yoshinuma, M. Kobayashi, S. Murakami, M. Goto, Y. Takeiri, D. Reiter, S. Okamura, and LHD Experimental Group, Plasma Fusion Res. **5**, S2099 (2011).
[34]S. S. Medley, D. Liu, M. V. Gorelenkova, W. W. Heidbrink, and L. Stagner, "Implementation of a 3D halo neutral model in the TRANSP code and application to projected NSTX-U plasmas," PPPL Report No. 5177, 2015.
[35]A. S. Tremsin and O. H. W. Siegmund, Proc. SPIE **3765**, 429 (1999).
[36]M. Fogle, D. Wulf, K. Morgan, D. McCammon, D. G. Seely, I. N. Draganic, and C. C. Havener, Phys. Rev. A **89**, 042705 (2014).
[37]M. Trassinelli, C. Prigent, E. Lamour, F. Mezdari, J. Mérot, R. Reuschl, J. P. Rozet, S. Steydli, and D. Vernhet, J. Phys. B: At., Mol. Opt. Phys. **45**, 085202 (2012).